

# Acoustically Driving the Single-Quantum Spin Transition of Diamond Nitrogen-Vacancy Centers

H. Y. Chen<sup>1</sup>, S. A. Bhave<sup>2</sup>, and G. D. Fuchs<sup>1,\*</sup>

<sup>1</sup>Cornell University, Ithaca, New York 14853, USA

<sup>2</sup>Purdue University, West Lafayette, Indiana 47907, USA



(Received 6 March 2020; accepted 4 May 2020; published 27 May 2020)

Using a high quality factor 3 GHz bulk acoustic wave resonator device, we demonstrate the acoustically driven single quantum spin transition ( $|m_s = 0\rangle \leftrightarrow |\pm 1\rangle$ ) for diamond nitrogen-vacancy (N-V) centers and characterize the corresponding stress susceptibility. A key challenge is to disentangle the unintentional magnetic driving field generated by the device current from the intentional stress driving within the device. We quantify these driving fields independently using Rabi spectroscopy before studying the more complicated case in which both are resonant with the single quantum spin transition. By building an equivalent circuit model to describe the device's current and mechanical dynamics, we quantitatively model the experiment to establish their relative contributions and compare with our results. We find that the stress susceptibility of the N-V center spin single quantum transition is around  $\sqrt{2}(0.5 \pm 0.2)$  times that for double quantum transition ( $|+1\rangle \leftrightarrow |-1\rangle$ ). Although acoustic driving in the double quantum basis is valuable for quantum-enhanced sensing applications, double quantum driving lacks the ability to manipulate N-V center spins out of the  $|m_s = 0\rangle$  initialization state. Our results demonstrate that efficient all-acoustic quantum control over N-V centers is possible, and is especially promising for sensing applications that benefit from the compact footprint and location selectivity of acoustic devices.

DOI: 10.1103/PhysRevApplied.13.054068

## I. INTRODUCTION

Acoustic control of solid-state quantum defect center spins [1–9], such as nitrogen-vacancy (N-V) centers in diamond [10], provides an additional resource for quantum control and coherence protection that is not available when using an oscillating magnetic field alone [11,12]. It also creates a path towards the construction of a hybrid quantum mechanical system [13] in which a defect center spin directly couples to a phonon mode of the host resonator. For diamond N-V centers, there has been substantial effort to understand the phonon-driven double quantum (DQ) spin transition ( $|m_s = +1\rangle \leftrightarrow |-1\rangle$ ) [1,4], including a measurement of the corresponding stress susceptibility,  $b$  [3,12]. In contrast, the phonon-driven single quantum (SQ) spin transition, with its associated stress susceptibility,  $b'$ , remains a missing puzzle piece in the full characterization of the N-V center ground-state spin-stress Hamiltonian. A recent calculation [14] suggests that  $|b'/b| < 0.1$ , which remains to be verified in experiments. Quantification of the phonon-driven SQ spin transition is important because SQ acoustic driving can enable all-acoustic quantum control of the N-V center electron spin, which can have an impact in real-world sensing applications. Given that the

solid-state phonon wavelength is  $10^4$  times shorter than that of a microwave photon at the same frequency, acoustic wave devices also support higher resolution, selective local spin control. Additionally, acoustic devices can be engineered with a smaller footprint and with potentially lower power consumption.

Here we report our experimental study of acoustically driven SQ spin transitions of N-V centers using a 3 GHz diamond bulk acoustic resonator device [15]. The device converts a microwave driving voltage into an acoustic wave through a piezoelectric transducer, thus mechanically addressing the N-V centers in the bulk diamond substrate. Because a microwave current flows through the device transducer, an oscillating magnetic field of the same frequency coexists with the stress field that couples to SQ spin transitions. To identify and quantify the mechanical contribution to the SQ spin transition, we use Rabi spectroscopy to separately quantify the magnetic and stress fields present in our device as a function of the driving frequency. Based on these results, we construct a theoretical model and simulate the SQ spin transition Rabi spectroscopy to compare to the experimental results. From a systematically identified closest match, we quantify the mechanical driving field contribution and extract the effective spin-stress susceptibility,  $b'$ . We perform measurements on both the  $|0\rangle \leftrightarrow |+1\rangle$  and  $|0\rangle \leftrightarrow |-1\rangle$  SQ spin transitions and obtain

\*gdf9@cornell.edu

$|b'/b| = \sqrt{2}(0.5 \pm 0.2)$ , around an order of magnitude larger than predicted by theory [14].

## II. EXPERIMENTAL SETUP AND THEORETICAL MODEL

The ground-state electron spin of a N-V center can be described by the Hamiltonian [14]

$$H_e/h = DS_z^2 + \gamma_e \mathbf{B} \cdot \mathbf{S} + H_\sigma/h, \quad (1)$$

where  $h$  is the Planck constant,  $D = 2.87$  GHz is the zero field splitting,  $\mathbf{S} = (S_x, S_y, S_z)$  is the vector of spin-1 Pauli matrices.  $\gamma_e = 2.802$  MHz/G is the spin gyromagnetic ratio in response to an external magnetic field,  $\mathbf{B} = (B_x, B_y, B_z)$ , and  $H_\sigma$  is a measure of the electron spin-stress interaction.

As shown in Fig. 1(a), in the presence of an external magnetic field aligned along the N-V axis,  $B_\parallel = B_z$ , the  $|\pm 1\rangle$  levels split linearly with the magnetic field amplitude due to the Zeeman effect. This gives rise to three sets of qubits of two types: (1)  $\{|0\rangle, |+1\rangle\}$  and  $\{|0\rangle, |-1\rangle\}$  operated on a SQ transition; (2)  $\{|+1\rangle, |-1\rangle\}$  operated on the DQ transition. While the magnetic dipole transition is accessible only for SQ transitions, phonons can drive both SQ and DQ transitions [14].

In our experiments, uniaxial stress fields,  $\sigma_{ZZ}$ , are generated along the [001] diamond crystal direction [see Fig. 1(b)]. This induces normal strain in the crystal,  $\{\epsilon_{XX}, \epsilon_{YY}, \epsilon_{ZZ}\} = \{-\nu\sigma_{ZZ}, -\nu\sigma_{ZZ}, \sigma_{ZZ}\}/E$ , where  $E$  is Young's modulus and  $\nu$  is Poisson's ratio. For simplicity, we work with the stress frame and the following stress Hamiltonian applies:

$$H_\sigma = H_{\sigma 0} + H_{\sigma 1} + H_{\sigma 2}, \quad (2a)$$

$$H_{\sigma 0}/h = a_1 \sigma_{ZZ} S_z^2, \quad (2b)$$

$$H_{\sigma 1}/h = 2b' \sigma_{ZZ} \{S_x, S_z\}, \quad (2c)$$

$$H_{\sigma 2}/h = 2b \sigma_{ZZ} (S_y^2 - S_x^2). \quad (2d)$$

Here  $a_1$ ,  $b'$ , and  $b$  are stress susceptibility coefficients, where  $a_1 = 4.4 \pm 0.2$  MHz/GPa and  $b = -2.3 \pm 0.3$  MHz/GPa have been experimentally measured [16], while  $b'$  has yet to be characterized. Theory predicts  $|b| \gg b' = 0.12 \pm 0.01$  MHz/GPa [14]. After applying the rotating wave approximation, the total Hamiltonian written in matrix form on the basis  $\{|+1\rangle, |0\rangle, |-1\rangle\}$  is

$$H_e = \begin{pmatrix} D + \gamma_e B_\parallel + a_1 \sigma_{ZZ} & \frac{1}{2} \Omega_1^+ e^{-i\omega t} & \frac{1}{2} \Omega_2 e^{-i\omega t} \\ \frac{1}{2} \Omega_1^+ e^{i\omega t} & 0 & \frac{1}{2} \Omega_1^- e^{i\omega t} \\ \frac{1}{2} \Omega_2 e^{i\omega t} & \frac{1}{2} \Omega_1^- e^{-i\omega t} & D - \gamma_e B_\parallel + a_1 \sigma_{ZZ} \end{pmatrix}, \quad (3)$$

where  $\omega = 2\pi f$  is the driving field frequency,  $\Omega_1^\pm = |\Omega_B \pm \Omega_{\sigma 1}| = 2|\gamma_e \mathbf{B}_\perp \cdot \mathbf{S} \pm \sqrt{2}b' \sigma_{ZZ}|$  is the SQ transition

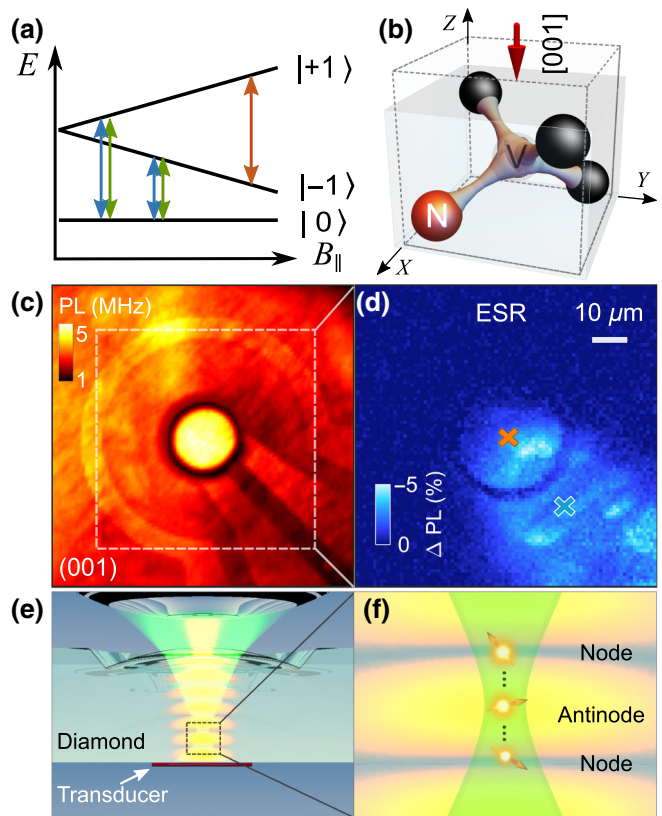


FIG. 1. (a) Ground-state spin levels of a N-V center as a function of the axial magnetic field. The orange and green arrows represent acoustically addressable qubit transitions and blue arrows represent magnetically addressable qubit transitions. The green arrows indicate the acoustically driven SQ spin transition under study. (b) Schematics showing uniaxial stress along the diamond [001] crystal axis applied to a N-V center (orientation  $[1\bar{1}\bar{1}]$ ), generated from the longitudinal acoustic wave mode of the resonator. (c) Photoluminescence scan of the device, consisting of a confocal diamond bulk acoustic resonator (center bright region) and a 50- $\mu\text{m}$ -radius microwave loop antenna. (d) Electron spin resonance signal mapping of the device current field around the resonator, showing current flow primarily along the electrodes. The local contrast change in signal intensity is due to fluorescence background variations. Crosses mark the locations under investigation in the experiments. (e) Cross-sectional view of the device. An NA = 0.8 microscope objective focuses the 532 nm laser down into diamond at a depth close to the transducer (around 3  $\mu\text{m}$  in distance). The orange standing wave field illustrates the acoustic wave mode. (f) Closeup of the area under study [orange cross in (d)]. The interrogated N-V ensemble distributes across the node and antinode of the acoustic wave.

Rabi field amplitude,  $\Omega_B$  and  $\Omega_\sigma$  are complex Rabi fields from the transverse magnetic field in microwave driving,  $\mathbf{B}_\perp$ , and the acoustic wave field,  $\sigma_{ZZ}$ , respectively, and  $\Omega_2 = |\Omega_{\sigma 2}| = 4b \sigma_{ZZ}$  represents the acoustically driven DQ transition Rabi field amplitude.

Experimentally, we fabricate a confocal bulk acoustic resonator device on a 20  $\mu\text{m}$  thick optical grade

diamond substrate [(001) face orientation, N-V center density approximately  $2 \times 10^{13} \text{ cm}^{-3}$ ] to launch longitudinal acoustic waves along the diamond [001] crystal axis at two mechanical resonance frequencies,  $f_r = 3.132 \text{ GHz}$  and  $2.732 \text{ GHz}$ . This allows phonon driving of both  $|0\rangle \leftrightarrow |+1\rangle$  and  $|0\rangle \leftrightarrow |-1\rangle$  SQ transitions as well as the  $|+1\rangle \leftrightarrow |-1\rangle$  DQ transition. At room temperature, we use a focused 532 nm laser (0.5 mW) to excite N-V centers in the substrate and collect their fluorescence from phonon side bands (greater than 675 nm) to detect their spin states using a home-built confocal microscope. A photoluminescence scan of the device along the  $X$ - $Y$  plane is shown in Fig. 1(c), featuring a micromechanical resonator (center bright circular area) encircled by a microwave loop antenna (radius approximately  $50 \mu\text{m}$ ). A detailed structural description and fabrication process of the device can be found in Ref. [15]. In Fig. 1(e) we show a schematic of the cross-sectional view of the device. The NA = 0.8 objective in our confocal microscope has a depth resolution around  $2.8 \mu\text{m}$  inside diamond, which is comparable to half of the acoustic wavelength,  $\lambda/2$ , and much smaller than that of the characteristic microwave magnetic field decay length.

Microwave (MW) driving of the piezoelectric transducer creates a bulk acoustic wave confined in the resonator and current-induced magnetic field throughout the device. On a spin resonance,  $f_{\text{MW}} = f_{|0\rangle \leftrightarrow |-1\rangle}$  or  $f_{\text{MW}} = f_{|0\rangle \leftrightarrow |+1\rangle}$ , the mixing of  $|0\rangle$  and  $|\pm 1\rangle$  spin states yields decreased photoluminescence (PL) from the N-V centers. The PL signal from the electron spin resonance (ESR) can thus be used to spatially map the current-induced magnetic field distribution in the device. In Fig. 1(d), with  $B_{\parallel} = 58 \text{ G}$ , we drive the transducer off resonance using a 2.715 GHz microwave source. The ESR measurement delineates the current field flowing through the leads and the resonator area. The acoustic wave field, however, is present only inside the resonator [see Fig. 1(e)] [15].

Given that the magnetic driving field,  $\mathbf{B}_{\perp}$ , and the acoustic driving field,  $\sigma_{zz}$ , coexist in the resonator and they both couple to the SQ spin transition, it is not possible to acoustically drive the N-V center SQ spin transition without magnetic driving field interference in our device. However, besides measuring the joint field effect on the SQ transition,  $\Omega_1^{\pm}$ , we can separately quantify the two field contributions using independent measurements on the two fields. More explicitly, the Rabi amplitude of the current-induced magnetic field inside the resonator [orange cross in Fig. 1(d)],  $\Omega_B$ , is proportional to that outside the resonator due to current continuity, and can be quantified by scaling the magnetic field  $\Omega'_B$  measured near the leads [blue cross in Fig. 1(d)] where the acoustic wave is absent, i.e.,  $\Omega_B = \beta \Omega'_B$ . The scaling factor  $\beta$  can be experimentally determined off a mechanical resonance frequency where the acoustic field is near zero. Because only phonon driving and not magnetic driving couples to the

DQ transition, the amplitude of the acoustic wave inside the resonator can be inferred by measuring the DQ transition Rabi field  $\Omega_{\sigma 2}$  [15], which is proportional to  $\Omega_{\sigma 1}$ , i.e.,  $\Omega_{\sigma 1} = \alpha \Omega_{\sigma 2} = |b'|/(\sqrt{2}b)|\Omega_{\sigma 2}|$ .

The phase properties of the two vector fields and the associated complex Rabi fields are complicated and evolve with frequency. The effect on  $\Omega_1^{\pm}$  depends on both resonator electromechanical characteristics and field spatial directions relative to the N-V atomic axis. We take into account the first part by determining an equivalent circuit of the device, and the second part by introducing an unknown constant parameter  $\phi$  to describe the phase difference of the two fields led by a spatial factor. The total SQ Rabi field as a function of driving frequency  $f$  is then

$$\Omega_1^{\pm}(f) = |\beta \Omega'_B(f) e^{i\phi} \pm \alpha \Omega_{\sigma 2}(f)|, \quad (4)$$

where  $\Omega(f) = \Omega(f) \exp[i\theta(f)]$ , and  $\theta(f)$  depends on resonator electromechanical characteristics.

### III. EXPERIMENTAL RESULTS AND DISCUSSION

#### A. SQ and DQ Rabi spectroscopy

We use SQ N-V center spin Rabi spectroscopy to measure  $\Omega'_B(f)$  at the marked blue cross location in Fig. 1(d). We first focus on the mechanical mode at  $f_r = 3.132 \text{ GHz}$ . In our experiment, we vary the N-V axial magnetic field  $B_{\parallel}$  around the point where the  $|0\rangle \leftrightarrow |+1\rangle$  transition frequency is close to  $f_r$  [see Fig. 2(a1)]. At each value of  $B_{\parallel}$ , we correspondingly adjust our driving frequency to the Zeeman splitting to maintain a condition of on-resonance driving. After spin state initialization into the  $|0\rangle$  state using optical spin polarization, we drive Rabi oscillations by applying varying length pulses to the piezoelectric transducer with a power at 10 dbm. We limit the probed nuclear hyperfine levels to the  $m_I = +1$  subspace [see Fig. 2(b1)] by requiring  $\Omega'_B(f) < 1.2 \text{ MHz}$ , which is below the hyperfine coupling coefficient. We then measure the spin population's time evolution as a function of pulse duration  $\tau$  through a photoluminescence measurement at the end of the Rabi sequence [see the inset of Fig. 2(d1)]. A series of measurements are done as we vary  $B_{\parallel}$  and the corresponding resonant drive frequencies around  $f_r$ . To ensure time stability, we keep track of the probed location by active feedback to the objective position, and limit the drift in the probed volume to less than  $(0.1 \mu\text{m})^3$ . The measurement results are shown in Fig. 2(c1). Rabi frequencies can then be extracted from either fitting or by taking the peak Fourier component of the Rabi spectroscopy results, as shown in Fig. 2(d1), and they are directly proportional to the associated driving field amplitude,  $B_{\perp}(f)$ . By comparing the magnetically driven Rabi fields  $\Omega'_B$  and  $\Omega_B$  that are measured off the mechanical resonance frequency, we calculate  $\beta = 1.30 \pm 0.01$ .

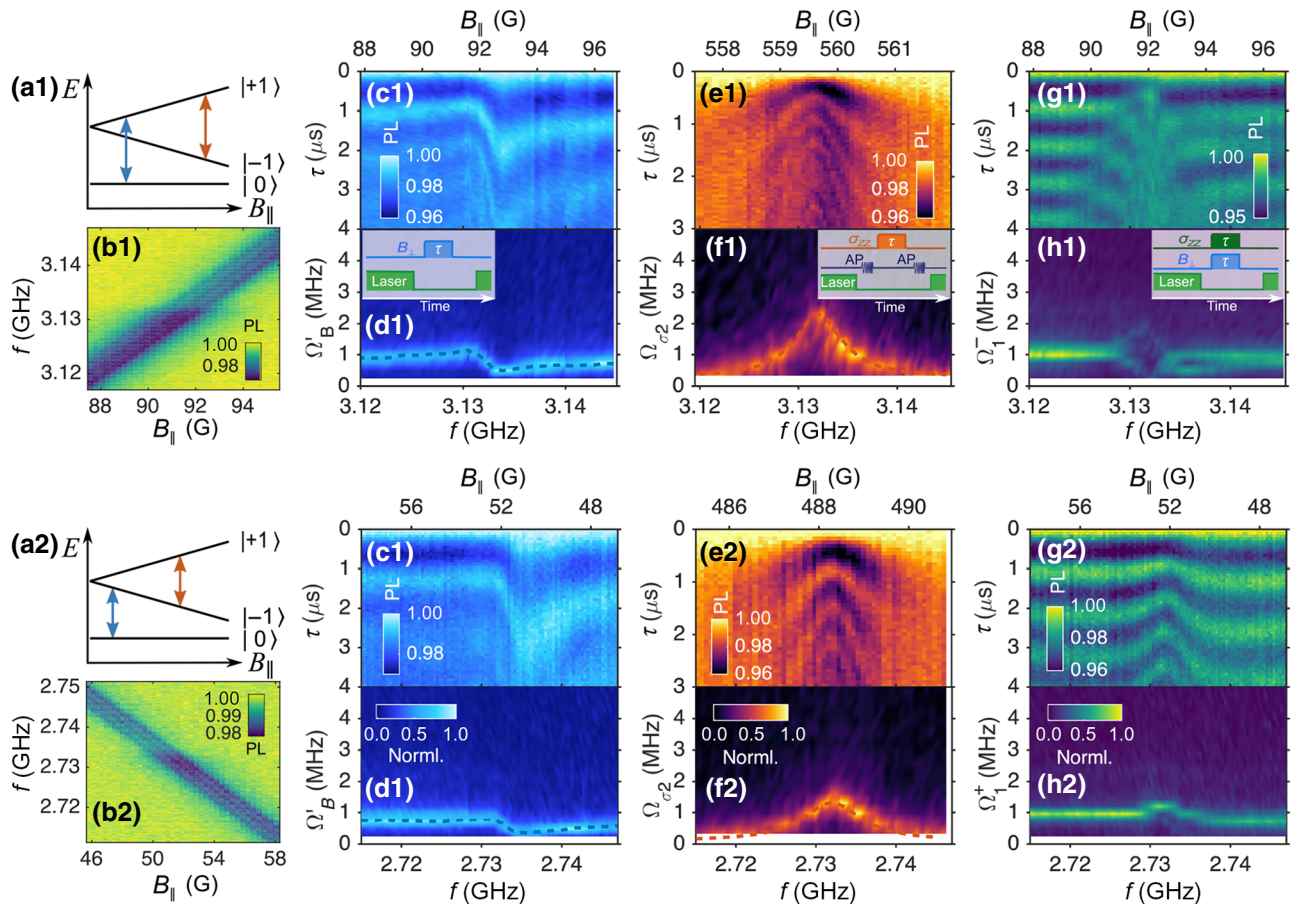


FIG. 2. Spectroscopy study of N-V center spin under driving fields at frequencies near two acoustic modes at (1) 3.132 GHz and (2) 2.732 GHz. Ground-state spin level diagrams in (a1) and (a2) show the targeted SQ (blue arrow,  $|0\rangle \leftrightarrow |\pm 1\rangle$ ) and DQ (orange arrow,  $|-1\rangle \leftrightarrow |+1\rangle$ ) transitions within a nuclear spin  $|m_I = +1\rangle$  hyperfine manifold. Transducer driving creates both magnetic,  $\mathbf{B}_\perp$ , and acoustic fields,  $\sigma_{zz}$ , in the device, which can be measured independently by (c) SQ Rabi spectroscopy near the leads [blue cross in Fig. 1(d)] and (e) DQ Rabi spectroscopy in the center of the resonator [orange cross in Fig. 1(d)]. In the resonator, the two vector fields add coherently and drive the SQ transition together. Measurements of the resulting total field probed by SQ ESR and Rabi spectroscopy are shown in (b) and (g), respectively. (d),(f),(h) Fourier transforms of (c),(e),(g). The insets in (d1),(f1),(h1) show the corresponding measurement sequences. Norml. is short for normalized value. AP stands for adiabatic passage pulse.

We perform similar Rabi spectroscopy on the  $|-1\rangle \leftrightarrow |+1\rangle$  DQ transition to measure  $\Omega_{\sigma_2}(f)$  at the marked orange cross location in Fig. 1(d), and target at a depth around  $3 \mu\text{m}$  from the transducer [see Fig. 1(e)]. From PL measurements of the N-V center ensemble in comparison to the single N-V center PL rate in our setup, we estimate around 150(20) N-V centers in the laser focal spot, among which approximately 35% of N-V centers are aligned with the external magnetic field  $B_\parallel$ . As a result, there are 45–60 N-V centers contributing to the signal, and they randomly span the node and antinode of the acoustic wave [see Fig. 1(f)]. The working axial magnetic field condition,  $B_\parallel \sim 560 \text{ G}$ , is close to the excited state level anticrossing (ELAC) [17] and provides near-perfect nuclear spin polarization in  $m_I = +1$ . In each resonant Rabi driving sequence [see the inset of Fig. 2(f1)], we use an adiabatic

passage pulse to prepare all spins into the  $|-1\rangle$  state. After resonant acoustic field driving, another adiabatic passage pulse is used to shelve the residual spin  $|-1\rangle$  population into  $|0\rangle$  prior to PL measurement. The results are shown in Figs. 2(e1) and 2(f1).

For SQ Rabi spectroscopy of  $\Omega'_B(f)$  measured at the leads, in Fig. 2(d1) we show two resonance features: the mechanical resonance at  $f_r = 3.132 \text{ GHz}$  and an electrical antiresonance at  $f_a = 3.134 \text{ GHz}$ , which originate from the electromechanical coupling of the piezoelectric resonator [18]. The result is consistent with the device admittance measurement using a vector network analyser (see Appendix B), and is used later towards the construction of a unique circuit model to describe the complex electromechanical response of our device. For DQ Rabi spectroscopy on  $\Omega_{\sigma_2}(f)$ , Fig. 2(f1) reveals a single Lorentzian

mechanical resonance at  $f_r = 3.132$  GHz, which corresponds to the longitudinal acoustic standing wave mode in the resonator. The modal mechanical quality factor,  $Q$ , can be directly calculated from the linewidth, which turns out to be around 1040(40). [Note that the measured  $\Omega_{\sigma 2}(f)$ ) corresponds to the peak stress field amplitude, considering that a N-V center located near the acoustic wave node contributes little to the Rabi oscillation signal.]

Having characterized the electromechanical response of our device, we perform SQ Rabi spectroscopy inside the resonator at the same location as the DQ measurement [marked with an orange cross in Fig. 1(d)]. The total Rabi field  $\Omega_1^+(f)$  is complicated because  $\mathbf{B}_\perp$  and  $\sigma_{zz}$  jointly act on the transition, and the probed N-V center ensemble includes N-V centers coupled to both an antinode and a node of the acoustic wave [see Fig. 1(f)], introducing spatial inhomogeneity in  $\sigma_{zz}(f)$ . The result shown in Fig. 2(g1) is distinct from the previous single field measurements, and its Fourier transform in Fig. 2(h1) disperses into multiple components due to the spatial inhomogeneity of stress coupling to the ensemble. To understand the spectrum and characterize the mechanical contribution to the SQ spin transition, we model our experiment in the following sections to solve the problem. We also perform similar measurements on a different acoustic mode at  $f_r = 2.732$  GHz to probe the  $|0\rangle \leftrightarrow |-1\rangle$  SQ transition. The results for  $\Omega'_B(f)$ ,  $\Omega_{\sigma 2}(f)$ , and  $\Omega_1^-(f)$  are shown in Figs. 2(c2)–2(h2).

## B. Modeling magnetic and stress fields

The electromechanical response of a piezoelectric resonator like our device can be modeled using an electrical equivalent circuit known as the modified Butterworth–Van Dyke (MBVD) model [18,19]. In the MBVD circuit model (Fig. 3 inset), the resonator acoustic mode is treated as a damped mechanical oscillator modeled using an electrical  $R_m L_m C_m$  series circuit. The acoustic  $R_m L_m C_m$  circuit is then coupled in parallel to an electrical  $R_0 C_0$  branch representing the electrical capacitance and dielectric loss in the transducer. Lastly, a serial resistor,  $R_s$ , is introduced to take into account ohmic loss in the contact lines. Applying an external voltage driving source near the resonance frequency,  $f_r = 1/(2\pi\sqrt{L_m C_m})$ , can excite both current and acoustic fields in the circuit. More explicitly, the total current (or admittance,  $\mathbf{Y}$ ) in the circuit model is proportional to the induced magnetic field, and the complex voltage value  $\mathbf{V}$  across the capacitor  $C_m$  is proportional to the stress field generated in the device.

With  $\Omega'_B(f)$  and  $\Omega_{\sigma 2}(f)$  measured experimentally, we perform MBVD model fitting with all circuit parameters set free using the equations

$$\begin{aligned} \Omega'_B(f) &= A \times |\mathbf{Y}(R_m, L_m, C_m, R_0, C_0, R_s, f)|, \\ \Omega_{\sigma 2}(f) &= B \times |\mathbf{V}(R_m, L_m, C_m, R_0, C_0, R_s, f)|, \end{aligned} \quad (5)$$

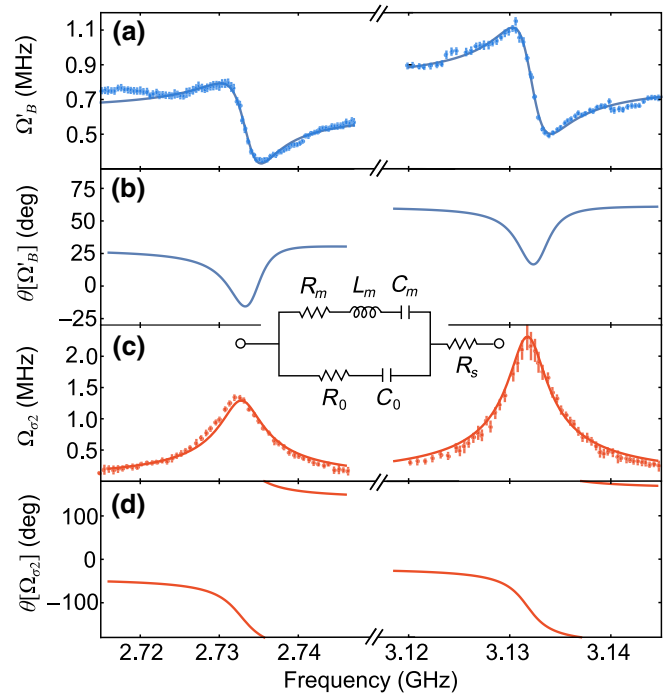


FIG. 3. Modeling device electromechanical characteristics through the modified Butterworth–Van Dyke model (inset), using  $\Omega'_B(f)$  and  $\Omega_{\sigma 2}(f)$  (blue and orange dots) as inputs. After fitting, the model yields both amplitude and phase information of the (a),(b) magnetic field and (c),(d) acoustic field.

where  $A$  and  $B$  are free scaling parameters. To simplify the modeling, we ignore other electrical components in the device, such as wire bond electrostatics and waveguide resonance.

The model fitting results are shown in Fig. 3, with the optimal fitting parameters as follows:  $\{A, B, R_m, L_m, C_m, R_0, C_0, R_s\} = \{235 \pm 155 \text{ MHz/S}, 2.6 \pm 0.1 \text{ kHz/V}, 219 \pm 165 \text{ Ω}, 13 \pm 9 \text{ μH}, 0.20 \pm 0.14 \text{ fF}, 46 \pm 30 \text{ Ω}, 0.20 \pm 0.13 \text{ pF}, 98 \pm 59 \text{ Ω}\}$  for the 3.132 GHz mode, and  $\{624 \pm 74 \text{ MHz/S}, 4.9 \pm 0.2 \text{ kHz/V}, 69 \pm 20 \text{ Ω}, 10 \pm 4 \text{ μH}, 0.33 \pm 0.13 \text{ fF}, 149 \pm 11 \text{ Ω}, 0.13 \pm 0.05 \text{ pF}, 732 \pm 86 \text{ Ω}\}$  for the 2.732 GHz mode. The large error bars are a result of the small covariance between the large number of fitting parameters; however, the model predictions of amplitude and phase are insensitive to these uncertainties. Thus, our model accurately represents the physical phenomena and is suitable for our purposes. The unified circuit model not only reproduces the measured Rabi field amplitude, but also contains the requisite phase information. While the acoustic field goes through a  $180^\circ$  phase change across a single mechanical resonance at  $f_r$ , the current field undergoes two resonances, where the phase first drops around  $f_r$  and then increases around  $f_a$ . From this analysis, we have full information of the complex Rabi fields,  $\Omega'_B(f)$  and  $\Omega_{\sigma 2}(f)$ .

### C. Simulation and extraction of SQ spin-stress susceptibility

To interpret Fig. 2(g), evaluate  $\alpha$ , and thus extract  $b'$ , we implement a quantum master equation simulation (see Appendix A) as a function of the driving frequency  $f$  for an ensemble of six N-V centers. We treat the ensemble as evenly distributed from an antinode ( $z = 0$ ) to a node ( $z = \lambda/4$ ) of the acoustic wave, driven by the SQ Rabi field

$$\Omega_1^\pm(f, z) = |1.3\Omega'_B(f)e^{i\phi} \pm \alpha\Omega_{\sigma 2}(f)\cos(kz)|, \quad (6)$$

where  $k = 2\pi/\lambda$ ,  $\lambda = 5.7 \mu\text{m}$  ( $6.7 \mu\text{m}$ ) for the  $f_r = 3.132 \text{ GHz}$  ( $2.732 \text{ GHz}$ ) mode. We sum the simulated time traces of the spin population from each individual N-V center and average to construct the final simulated Rabi spectroscopy result.

We implement simulations for a range of  $\{\alpha, \phi\}$  values and compare to the experimental data in Fig. 2(g) by calculating their structural similarity (SSIM) index (see Appendix A) [20]. The results are shown in Fig. 4(a). A higher SSIM value indicates a better simulation-to-experiment match. We find the best match at  $\{\alpha, \phi\} = \{0.5 \pm 0.2, 10^\circ \pm 40^\circ\}$  for the 2.732 GHz mode and  $\{\alpha, \phi\} = \{0.5 \pm 0.2, -60^\circ \pm 60^\circ\}$  for the 3.132 GHz mode. The corresponding simulated Rabi spectroscopy results are shown in Fig. 4(b), which agree well with experimental observation. Additionally, we obtain the same  $\alpha$  result from both modes, which is expected physically. The difference in  $\phi$  implies a phase change of  $\theta$  in electromechanical resonance or a direction change in the magnetic vector field,  $\mathbf{B}_\perp$ , between the two resonance modes, which can be explained by the microwave resonance in the transmission line (see Appendix B). From our result that  $\alpha = |b'|/(\sqrt{2}b) = 0.5 \pm 0.2$ , we find that the spin-stress susceptibility of the SQ transition compared to that of the DQ transition is  $|b'| = \sqrt{2}(0.5 \pm 0.2)|b|$ . This finding further completes our understanding of the N-V center ground-state spin-stress Hamiltonian. Note that  $b'$  describes spin coupling to only a normal stress field. The spin coupling to shear stress wave coefficient for the SQ transition,  $c'$ , is not measured (see Appendix C).

The fact that  $b'$  is comparable to  $b$ , about an order of magnitude larger than expected, has important implications for applications. It raises the possibility of all-acoustic spin control of N-V centers within their full spin manifold without the need for a magnetic antenna. For sensing applications, a diamond bulk acoustic device can be practical and outperform a microwave antenna in several aspects: (1) Acoustic waves provide direct access to all three qubit transitions, and the DQ qubit enables better sensitivity in magnetic metrology applications [21]. (2) The micron-scale phonon wavelength is ideal for local selective spin control of N-V centers. (3) Bulk acoustic waves contain a uniform stress mode profile and thus allow uniform

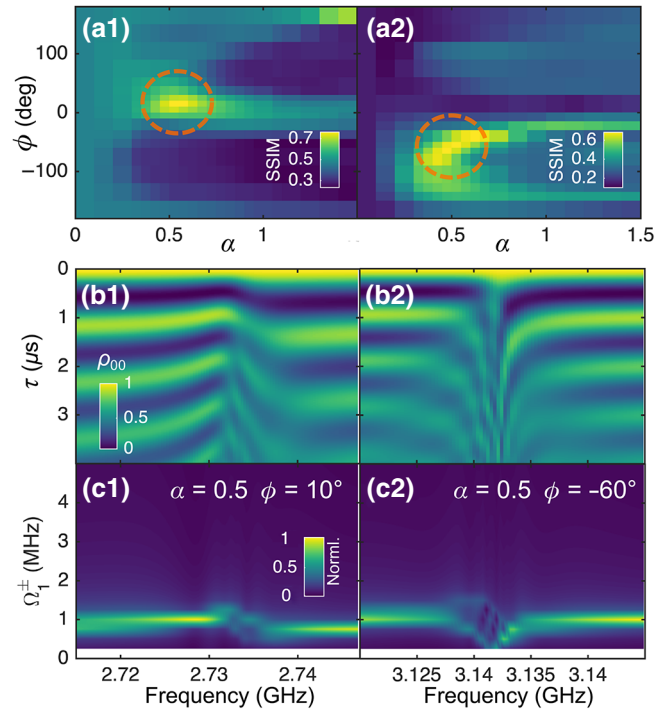


FIG. 4. Quantum master equation simulation of single quantum spin transition under dual field driving using model inputs from Fig. 3. (a1),(a2) Heatmaps of structural similarity index calculated between experimental data and simulation in  $\{\phi, \alpha\}$  parameter space for  $f_r = 2.732 \text{ GHz}$  and  $3.132 \text{ GHz}$  mode, respectively. The dashed circles mark the locations of peak SSIM values. (b1),(b2) The corresponding simulated Rabi spectroscopy results using the peak SSIM associated  $\{\phi, \alpha\}$  values match the experimental data in Figs. 2(g1) and 2(g2). (c1),(c2) Fourier transforms of (b1),(b2).

field control of a large planar spin ensemble, for example, from a delta-doped diamond growth process [22].

### IV. CONCLUSION

In summary, we experimentally study the acoustically driven single quantum spin transition of diamond N-V centers using a 3 GHz piezoelectric bulk acoustic resonator device. We observe the phonon-driven SQ spin transition, disentangled from the background driving microwave magnetic field. Through device circuit modeling and quantum master equation simulation of the N-V spin ensemble, we successfully reproduce the experimental results and extract the SQ transition spin-stress susceptibility, which is an order of magnitude higher than is theoretically predicted and further completes the characterization of the N-V spin-stress Hamiltonian. This study, combined with previously demonstrated phonon-driven DQ quantum control and improvements in diamond mechanical resonator engineering, shows that diamond acoustic devices are a powerful tool for full quantum state control of N-V center spins.

## ACKNOWLEDGMENTS

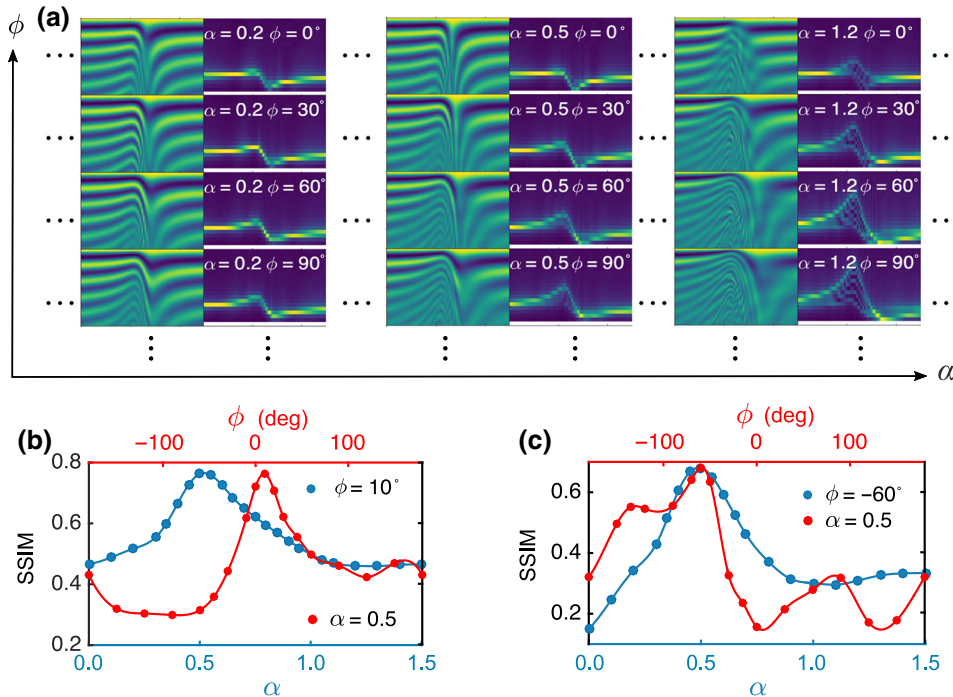
Research support was provided by the DARPA DRINQS program (Cooperative Agreement #D18A C00024) and by the Office of Naval Research (Grant No. N000141712290). Any opinions, findings, and conclusions or recommendations expressed in this publication are those of the author(s) and do not necessarily reflect the views of DARPA. Device fabrication was performed in part at the Cornell NanoScale Science and Technology Facility, a member of the National Nanotechnology Coordinated Infrastructure, which is supported by the National Science Foundation (Grant No. ECCS-15420819), and at the Cornell Center for Materials Research Shared Facilities that are supported through the NSF MRSEC program (Grant No. DMR-1719875).

## APPENDIX A: QUANTUM MASTER EQUATION SIMULATION

We perform numerical simulation of the experiment using the Lindblad master equation [23],

$$\dot{\rho} = -\frac{i}{\hbar}[H_e, \rho] + \sum_{i,j} \gamma_{ij} \left( L_i \rho L_j^\dagger - \frac{1}{2} \{L_i^\dagger L_j, \rho\} \right), \quad (\text{A1})$$

where  $\rho$  is the density matrix of the spin states,  $L$  is the Lindblad operator,  $i, j = +1, 0, -1$ . For the short time scope studied here,  $\tau \leq 4 \mu\text{s}$ , we ignore the longitudinal spin relaxation process, and set phase coherence  $T_2 = 1/\gamma_{ii} = 2 \mu\text{s}$ . We evolve the density matrix from a pure state of  $|0\rangle$ , i.e.,  $\rho(\tau = 0) = |0\rangle\langle 0|$ , and calculate the spin



population in  $\rho_{00}(\tau)$  to simulate the PL signal collected in the experiment.

Because the  $\{\alpha, \phi\}$  are unknown from direct experimental measurement, we perform a series of simulations in the range  $\alpha = (0, 1.5)$  and  $\phi = (-180^\circ, 180^\circ)$ , as shown in Fig. 5(a), which can be directly compared to the experiment. The evaluation of an experiment-simulation match is through the SSIM index,  $S_i$  [20]:

$$S_i(x, y) = \frac{(2\mu_x\mu_y + C_1)(2\sigma_{xy} + C_2)}{(\mu_x^2 + \mu_y^2 + C_1)(\sigma_x^2 + \sigma_y^2 + C_2)}. \quad (\text{A2})$$

Here  $\mu_x$ ,  $\mu_y$ ,  $\sigma_x$ ,  $\sigma_y$ , and  $\sigma_{xy}$  are the local means, standard deviations, and cross covariance for the two images,  $x$  and  $y$ , under comparison;  $C_1 = C_2/9 = (0.01L)^2$ , where  $L = 255$  is the dynamic range value of the image; SSIM = 0 indicates no structural similarity and SSIM = 1 indicates identical images. We choose to work with SSIM instead of other error sensitive approaches, such as the mean squared error, because SSIM is a perception-based model for image structural information, and the measurement is insensitive to average luminance and contrast change in the images.

We are unaware of a formally defined measure of the uncertainty estimation using SSIM in image assessment. For quantitative evaluation, here we report the uncertainty for  $\{\alpha, \phi\}$  by the half width at half maximum in normalized SSIM( $\alpha$ ) and SSIM( $\phi$ ). The results are shown in Figs. 5(b) and 5(c).

FIG. 5. (a) Quantum master equation simulation in  $\{\alpha, \phi\}$  space. (b),(c) Line cuts from the simulation results in Fig. 4(a) for the two resonance modes at  $f_r = 2.732$  and  $3.132$  GHz, respectively. Half width at half maximum of the peaks in the normalized curves are used to evaluate uncertainties in  $\alpha$  and  $\phi$ .

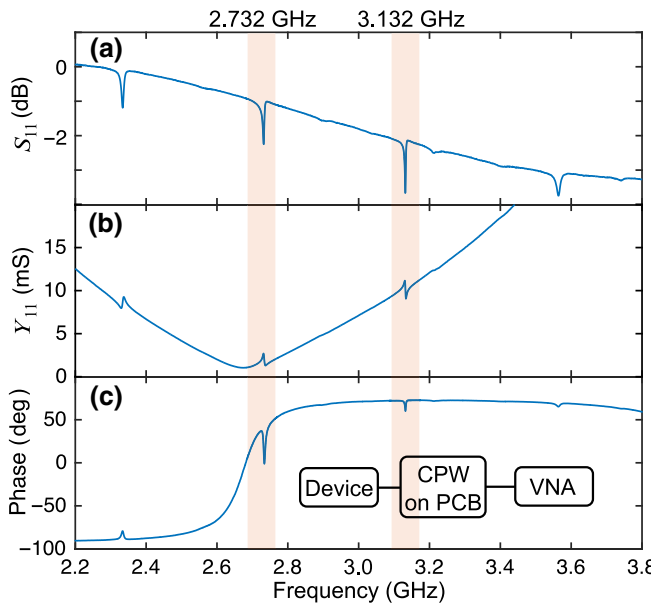


FIG. 6. Electrical  $S$ -parameter measurements of the device (wire bonded to a printed circuit board) using a vector network analyser, showing the (a) voltage reflection  $S_{11}$ , (b) amplitude, and (c) phase of admittance  $Y_{11}$  as a function of the driving frequency. The orange hue highlights the resonance modes under study. The inset in (c) shows the measurement scheme.

## APPENDIX B: ELECTRICAL CHARACTERIZATION OF DEVICE

In our experiment, the device is wire bonded to a coplanar waveguide (CPW) on a printed circuit board (PCB) for microwave driving. We electrically characterize the device-PCB complex using a vector network analyser (VNA). The results are shown in Fig. 6. The PCB waveguide quarter-wavelength resonance at around 2.66 GHz

distorts the device frequency response and introduces deviations from the standard MBVD model for the 2.732 GHz operating mode. We attribute this as the main cause for the small model fitting deviation from experimental data for  $f < 2.72$  GHz in Fig. 3(a).

We build our MBVD circuit model from Rabi field spectroscopy measurements instead of the electrical measurements because the electrical measurement results are more sensitive to the microwave transmission line configuration and calibrations. In contrast, N-V centers provide direct local measurement of both current and stress vector fields, and thus serve as a more accurate report of the device behavior.

## APPENDIX C: FULL SPIN-STRESS HAMILTONIAN AND STRAIN SUSCEPTIBILITY MAPPING

The full spin-stress Hamiltonian for a [111] oriented N-V center is [14,16]:

$$H_{\sigma 0}/h = \mathcal{M}_z S_z^2, \quad (C1a)$$

$$H_{\sigma 1}/h = \mathcal{N}_x \{S_x, S_z\} + \mathcal{N}_y \{S_y, S_z\}, \quad (C1b)$$

$$H_{\sigma 2}/h = \mathcal{M}_x (S_y^2 - S_x^2) + \mathcal{M}_y \{S_x, S_y\}, \quad (C1c)$$

where

$$\begin{aligned} \mathcal{M}_z = & a_1 (\sigma_{XX} + \sigma_{YY} + \sigma_{ZZ}) \\ & + 2a_2 (\sigma_{YZ} + \sigma_{ZX} + \sigma_{XY}), \end{aligned} \quad (C2a)$$

$$\begin{aligned} \mathcal{M}_x = & b (2\sigma_{ZZ} - \sigma_{XX} - \sigma_{YY}) \\ & + c (2\sigma_{XY} - \sigma_{YZ} - \sigma_{ZX}), \end{aligned} \quad (C2b)$$

$$\mathcal{M}_y = \sqrt{3} [b(\sigma_{XX} - \sigma_{YY}) + c(\sigma_{YZ} - \sigma_{ZX})], \quad (C2c)$$

TABLE I. N-V center ground-state spin coupling to stress and strain field coefficients.

	$a_1$ (MHz/GPa)	$a_2$ (MHz/GPa)	$b$ (MHz/GPa)	$c$ (MHz/GPa)	$b'$ (MHz/GPa)	$c'$ (MHz/GPa)
[16]	$4.4 \pm 0.2$	$-3.7 \pm 0.2$	$-2.3 \pm 0.3$	$3.5 \pm 0.3$	...	...
[24]	$-11.7 \pm 3.2$	$6.5 \pm 3.2$	$7.1 \pm 0.8$	$-5.4 \pm 0.8$	...	...
[14]	$2.66 \pm 0.07$	$-2.51 \pm 0.06$	$-1.94 \pm 0.02$	$2.83 \pm 0.03$	$0.12 \pm 0.01$	$-0.66 \pm 0.01$
	...	...	...	...	$\pm \sqrt{2}(0.5 \pm 0.2)b$	...
	$\lambda_{a_1}$ (GHz/strain)	$\lambda_{a_2}$ (GHz/strain)	$\lambda_b$ (GHz/strain)	$\lambda_c$ (GHz/strain)	$\lambda_{b'}$ (GHz/strain)	$\lambda_{c'}$ (GHz/strain)
[24]	$-0.5 \pm 8.6$	$-9.2 \pm 5.7$	$-0.5 \pm 1.2$	$14.0 \pm 1.3$	...	...
[14]	$2.3 \pm 0.2$	$-6.42 \pm 0.09$	$-1.425 \pm 0.050$	$4.915 \pm 0.022$	$0.65 \pm 0.02$	$-0.707 \pm 0.018$
	$d_{\parallel}$ (GHz/strain)	$d_{\perp}$ (GHz/strain)				
[3]	$5.46 \pm 0.31$	$19.63 \pm 0.40$				
[12]	$13.3 \pm 1.1$	$21.5 \pm 1.2$				

$$\mathcal{N}_x = b'(2\sigma_{ZZ} - \sigma_{XX} - \sigma_{YY}) + c'(2\sigma_{XY} - \sigma_{YZ} - \sigma_{ZX}), \quad (\text{C2d})$$

$$\mathcal{N}_y = \sqrt{3}[b'(\sigma_{XX} - \sigma_{YY}) + c'(\sigma_{YZ} - \sigma_{ZX})]. \quad (\text{C2e})$$

For the uniaxial stress field,  $\sigma_{ZZ}$ , only  $a_1$ ,  $b$ , and  $b'$  related coupling are excited, and the above equation reduces to Eq. (2). In order to probe  $c'$ , a shear stress field will be required (note that  $b'$  and  $c'$  are respectively named  $d$  and  $e$  in Ref. [14]), which can be generated from, for example, a uniaxial stress applied along the [110] crystal direction.

To map spin-stress susceptibility to spin-strain susceptibility, we can apply the stress-to-strain tensor transformation to Eq. (C2) using the elastic stiffness tensor  $C$ . The resulting spin-strain coupling written in the N-V axis frame ( $x = [-1, -1, 2]/\sqrt{6}$ ,  $y = [1, -1, 0]/\sqrt{2}$ ,  $z = [1, 1, 1]/\sqrt{3}$ ) is [24]

$$\mathcal{M}_z = \lambda_{a1}\epsilon_{zz} + \lambda_{a2}(\epsilon_{xx} + \epsilon_{yy}), \quad (\text{C3a})$$

$$\mathcal{M}_x = \lambda_b(\epsilon_{xx} - \epsilon_{yy}) + 2\lambda_c\epsilon_{xz}, \quad (\text{C3b})$$

$$\mathcal{M}_y = -2\lambda_b\epsilon_{xy} + 2\lambda_c\epsilon_{yz}, \quad (\text{C3c})$$

$$\mathcal{N}_x = \lambda_b(\epsilon_{xx} - \epsilon_{yy}) + 2\lambda_c\epsilon_{xz}, \quad (\text{C3d})$$

$$\mathcal{N}_y = -2\lambda_{b'}\epsilon_{xy} + 2\lambda_{c'}\epsilon_{yz}, \quad (\text{C3e})$$

where

$$\lambda_{a1} = a_1(C_{11} + 2C_{12}) + 4a_2C_{44}, \quad (\text{C4a})$$

$$\lambda_{a2} = a_1(C_{11} + 2C_{12}) - 2a_2C_{44}, \quad (\text{C4b})$$

$$\lambda_b = b(C_{11} - C_{12}) + 2cC_{44}, \quad (\text{C4c})$$

$$\lambda_c = \sqrt{2}[b(C_{11} - C_{12}) - cC_{44}], \quad (\text{C4d})$$

$$\lambda_{b'} = b'(C_{11} - C_{12}) + 2c'C_{44}, \quad (\text{C4e})$$

$$\lambda_{c'} = \sqrt{2}[b'(C_{11} - C_{12}) - c'C_{44}], \quad (\text{C4f})$$

$C_{11} = 1079 \pm 5$  GPa,  $C_{12} = 124 \pm 5$  GPa, and  $C_{44} = 578 \pm 2$  GPa [25].

Experimentally and theoretically characterized mechanical coupling coefficients are summarized in Table I. Note that early experimental characterization [3, 12] parameterized the coefficients as coupling to N-V axial strain  $d_{\parallel}$  and transverse strain coupling  $d_{\perp}$ , instead of the tensor component representation as described above.

#### APPENDIX D: COMSOL SIMULATION OF MAGNETIC AND ELECTRIC FIELDS IN THE DEVICE

Apart from magnetic and acoustic fields, an oscillating electric field from the current discharge in our device can be a potential driving source for the spin transition. To quantify the electric field in the device, we perform a COMSOL simulation where the transducer is modeled

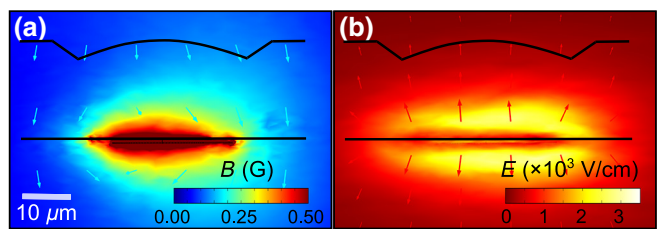


FIG. 7. COMSOL simulation of the (a) magnetic field and (b) electric field generated from the piezoelectric transducer modeled as a capacitor.

as a capacitor. We adjust the driving voltage source ( $f = 3$  GHz) such that the generated  $B$  field at the experimentally interrogated location is around 0.3 G and the corresponding Rabi field is  $\Omega_B = \sqrt{2}\gamma_e B \sim 1.2$  MHz, as shown in Fig. 7(a).

Under the same conditions, we plot the simulated electric field distribution in Fig. 7(b). The amplitude of the electric field is around  $2 \times 10^3$  V/cm. Using the known DQ spin-electric field susceptibility,  $d_{\perp} = 17$  Hz cm/V [26], the corresponding electric Rabi field amplitude is  $\Omega_E = 2d_{\perp}E < 0.1$  MHz, which is negligible in our experiment.

- [1] E. R. MacQuarrie, T. A. Gosavi, N. R. Jungwirth, S. A. Bhave, and G. D. Fuchs, Mechanical Spin Control of Nitrogen-Vacancy Centers in Diamond, *Phys. Rev. Lett.* **111**, 227602 (2013).
- [2] E. MacQuarrie, T. Gosavi, A. Moehle, N. Jungwirth, S. Bhave, and G. Fuchs, Coherent control of a nitrogen-vacancy center spin ensemble with a diamond mechanical resonator, *Optica* **2**, 233 (2015).
- [3] J. Teissier, A. Barfuss, P. Appel, E. Neu, and P. Maletinsky, Strain Coupling of a Nitrogen-Vacancy Center Spin to a Diamond Mechanical Oscillator, *Phys. Rev. Lett.* **113**, 020503 (2014).
- [4] A. Barfuss, J. Teissier, E. Neu, A. Nunnenkamp, and P. Maletinsky, Strong mechanical driving of a single electron spin, *Nat. Phys.* **11**, 820 (2015).
- [5] D. A. Golter, T. Oo, M. Amezcuia, K. A. Stewart, and H. Wang, Optomechanical Quantum Control of a Nitrogen-Vacancy Center in Diamond, *Phys. Rev. Lett.* **116**, 143602 (2016).
- [6] K. W. Lee, D. Lee, P. Ovartchaiyapong, J. Minguzzi, J. R. Maze, and A. C. B. Jayich, Strain Coupling of a Mechanical Resonator to a Single Quantum Emitter in Diamond, *Phys. Rev. Appl.* **6**, 034005 (2016).
- [7] H. Y. Chen, E. MacQuarrie, and G. D. Fuchs, Orbital State Manipulation of a Diamond Nitrogen-Vacancy Center Using a Mechanical Resonator, *Phys. Rev. Lett.* **120**, 167401 (2018).
- [8] S. J. Whiteley, G. Wolfowicz, C. P. Anderson, A. Bourassa, H. Ma, M. Ye, G. Koolstra, K. J. Satzinger, M. V. Holt, F. J. Heremans, A. N. Cleland, D. I. Schuster, G. Galli, and D. D. Awschalom, Spin-phonon interactions in silicon carbide addressed by Gaussian acoustics, *Nat. Phys.* **15**, 490 (2019).

- [9] S. Maity, L. Shao, S. Bogdanovic, S. Meesala, Y.-I. Sohn, N. Sinclair, B. Pingault, M. Chalupnik, C. Chia, L. Zheng, K. Lai, and M. Loncar, Coherent acoustic control of a single silicon vacancy spin in diamond, *Nat. Commun.* **11**, 1 (2020).
- [10] M. W. Doherty, N. B. Manson, P. Delaney, F. Jelezko, J. Wrachtrup, and L. C. Hollenberg, The nitrogen-vacancy colour centre in diamond, *Phys. Rep.* **528**, 1 (2013).
- [11] E. MacQuarrie, T. Gosavi, S. Bhave, and G. Fuchs, Continuous dynamical decoupling of a single diamond nitrogen-vacancy center spin with a mechanical resonator, *Phys. Rev. B* **92**, 224419 (2015).
- [12] P. Ovartchayapong, K. W. Lee, B. A. Myers, and A. C. B. Jayich, Dynamic strain-mediated coupling of a single diamond spin to a mechanical resonator, *Nat. Commun.* **5**, 4429 (2014).
- [13] J. Cady, O. Michel, K. Lee, R. Patel, C. J. Sarabalis, A. H. Safavi-Naeini, and A. B. Jayich, Diamond optomechanical crystals with embedded nitrogen-vacancy centers, *Quantum Sci. Technol.* **4**, 024009 (2019).
- [14] P. Udvarhelyi, V. O. Shkolnikov, A. Gali, G. Burkard, and A. Pályi, Spin-strain interaction in nitrogen-vacancy centers in diamond, *Phys. Rev. B* **98**, 075201 (2018).
- [15] H. Chen, N. F. Oondo, B. Jiang, E. R. MacQuarrie, R. S. Daveau, S. A. Bhate, and G. D. Fuchs, Engineering electron–phonon coupling of quantum defects to a semiconfocal acoustic resonator, *Nano Lett.* **19**, 7021 (2019).
- [16] M. S. Barson, P. Peddibhotla, P. Ovartchayapong, K. Ganeshan, R. L. Taylor, M. Gebert, Z. Mielens, B. Koslowski, D. A. Simpson, L. P. McGuinness, J. McCallum, S. Prawer, S. Onoda, T. Ohshima, A. C. Bleszynski Jayich, F. Jelezko, N. B. Manson, and M. W. Doherty, Nanomechanical sensing using spins in diamond, *Nano Lett.* **17**, 1496 (2017).
- [17] V. Jacques, P. Neumann, J. Beck, M. Markham, D. Twitchen, J. Meijer, F. Kaiser, G. Balasubramanian, F. Jelezko, and J. Wrachtrup, Dynamic Polarization of Single Nuclear Spins by Optical Pumping of Nitrogen-Vacancy Color Centers in Diamond at Room Temperature, *Phys. Rev. Lett.* **102**, 057403 (2009).
- [18] C. C. Enz and A. Kaiser, *MEMS-Based Circuits and Systems for Wireless Communication* (Springer Science & Business Media, New York, 2012).
- [19] Standard Definitions Methods of measurement for piezoelectric vibrators, IEEE Std 177-1966.
- [20] Z. Wang, A. C. Bovik, H. R. Sheikh, and E. P. Simoncelli, Image quality assessment: From error visibility to structural similarity, *IEEE Trans. Image Process.* **13**, 600 (2004).
- [21] J. Taylor, P. Cappellaro, L. Childress, L. Jiang, D. Budker, P. Hemmer, A. Yacoby, R. Walsworth, and M. Lukin, High-sensitivity diamond magnetometer with nanoscale resolution, *Nat. Phys.* **4**, 810 (2008).
- [22] K. Ohno, F. Joseph Heremans, L. C. Bassett, B. A. Myers, D. M. Toyli, A. C. Bleszynski Jayich, C. J. Palmstrøm, and D. D. Awschalom, Engineering shallow spins in diamond with nitrogen delta-doping, *Appl. Phys. Lett.* **101**, 082413 (2012).
- [23] H.-P. Breuer F. Petruccione *et al.*, *The Theory of Open Quantum Systems* (Oxford University Press on Demand, New York, 2002).
- [24] A. Barfuss, M. Kasperczyk, J. Kölbl, and P. Maletinsky, Spin-stress and spin-strain coupling in diamond-based hybrid spin oscillator systems, *Phys. Rev. B* **99**, 174102 (2019).
- [25] H. McSkimin, P. Andreatch, Jr., and P. Glynn, The elastic stiffness moduli of diamond, *J. Appl. Phys.* **43**, 985 (1972).
- [26] E. Van Oort and M. Glasbeek, Electric-field-induced modulation of spin echoes of N-V centers in diamond, *Chem. Phys. Lett.* **168**, 529 (1990).